MOLECULAR IMAGING AND BIOLOGY

Mol Imaging Biol (2020)
DOI: 10.1007/s11307-020-01491-y

WMIS World Molecular Imaging Society
esmi European Society for Molecular Imaging

RESEARCH ARTICLE

SimPET: a Preclinical PET Insert for Simultaneous PET/MR Imaging

Jeong-Whan Son,[1] Kyeong Yun Kim,[1,2,3] Ji Yong Park,[2,3] Kyuwan Kim,[1] Yun-Sang Lee,[3] Guen Bae Ko,[1,3] Jae Sung Lee[1,2,3]

[1]*Brightonix Imaging Inc., Yeonmujang 5ga-gil, Seongdong-gu, Seoul, 04782, South Korea*
[2]*Department of Biomedical Sciences, Seoul National University College of Medicine, 103 Daehak-ro, Jongno-gu, Seoul, 03080, South Korea*
[3]*Department of Nuclear Medicine, Seoul National University College of Medicine, 103 Daehak-ro, Jongno-gu, Seoul, 03080, South Korea*

Abstract

Purpose: SimPET/M7 system is a small-animal dedicated simultaneous positron emission tomography and magnetic resonance imaging (PET/MRI) scanner. The SimPET insert has been upgraded from its prototype with a focus on count rate performance and sensitivity. The M7 scanner is a 1-T permanent magnet-based compact MRI system without any cryogens. Here, we present performance evaluation results of SimPET along with the results of mutual interference evaluation and simultaneously acquired PET/MR imaging.

Procedures: Following NEMA NU 4-2008 standard, we evaluated the performance of the SimPET system. The M7 MRI compatibility of SimPET was also assessed by analyzing MRI images of a uniform phantom under different PET conditions and PET count rates with different MRI pulse sequences. Mouse imaging was performed including a whole-body ^{18}F-NaF PET scan and a simultaneous PET/MRI scan with ^{64}Cu-NOTA-ironoxide.

Results: The spatial resolution at center based on 3D OSEM without and with warm background was 0.7 mm and 1.45 mm, respectively. Peak sensitivity was 4.21 % (energy window = 250–750 keV). The peak noise equivalent count rate with the same energy window was 151 kcps at 38.4 MBq. The uniformity was 4.42 %, and the spillover ratios in water- and air-filled chambers were 14.6 % and 12.7 %, respectively. In the hot rod phantom image, 0.75-mm-diameter rods were distinguishable. There were no remarkable differences in the SNR and uniformity of MRI images and PET count rates with different PET conditions and MRI pulse sequences. In the whole-body ^{18}F-NaF PET images, fine skeletal structures were well resolved. In the simultaneous PET/MRI study with ^{64}Cu-NOTA-ironoxide, both PET and MRI signals changed before and after injection of the dual-modal imaging probe, which was evident with the exact spatiotemporal correlation.

Conclusions: We demonstrated that the SimPET scanner has a high count rate performance and excellent spatial resolution. The combined SimPET/M7 enabled simultaneous PET/MR imaging studies with no remarkable mutual interference between the two imaging modalities.

Key words: PET/MRI, Simultaneous imaging, NEMA performance

Jeong-Whan Son and Kyeong Yun Kim contributed equally to this work.
Electronic supplementary material The online version of this article (https://doi.org/10.1007/s11307-020-01491-y) contains supplementary material, which is available to authorized users.

Correspondence to: Guen Ko; *e-mail:* gbko@brtnx.com, Jae Lee; *e-mail:* jaes@snu.ac.kr

Published online: 13 April 2020

Introduction

In vivo imaging of small animals using state-of-the-art imaging devices has enabled the investigation of

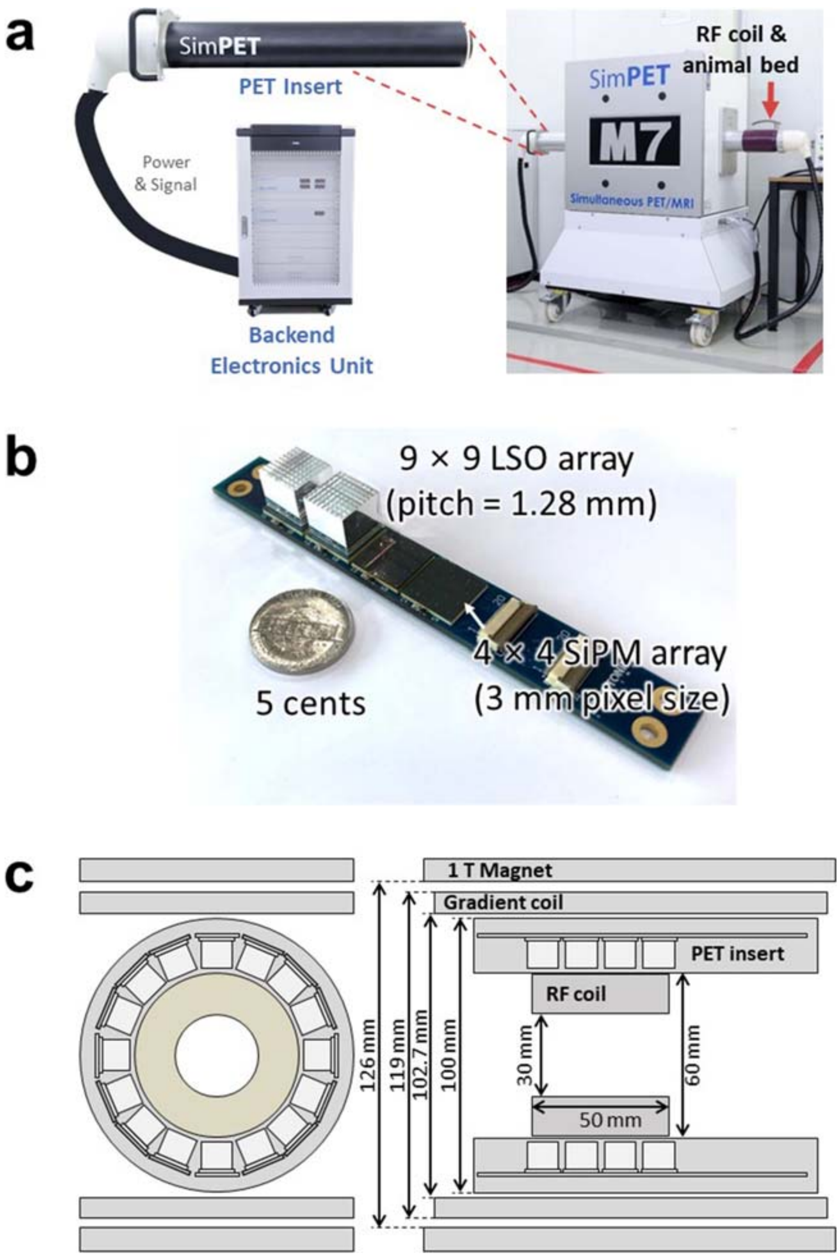

Fig. 1. SimPET system for simultaneous PET/MR imaging. **a** SimPET insert and its backend electronics unit with M7 preclinical MRI scanner. **b** PET detector comprising LSO blocks and SiPMs. **c** A schematic drawing of the cross-sectional view of the PET/MRI system with the major sizes.

biological processes of diseases and the elucidation of the effectiveness of new drugs and therapies [1–5]. Positron emission tomography (PET) is one of the most widely used biomedical imaging techniques to study metabolic pathways and diseases because PET systems provide images with the highest (*i.e.*, picomolar) sensitivity among all *in vivo* imagers [6, 7]. Another advantage of a PET system is the quantitative information of the dynamic processes of interest that can be obtained by applying proper physical corrections [8]. PET and magnetic resonance imaging (MRI) can be combined to provide further information by complementing each other because MRI scanners offer high-resolution anatomical images with excellent soft-tissue contrast [9–12]. To fully utilize the advantages of combined PET/MRI (*e.g.*, near-perfect spatiotemporal correlation, minimized inter-modality motion, and reduced scan time), both images should be acquired simultaneously [13–15].

Recently, preclinical and clinical PET inserts with MRI compatibility have been developed for research purposes as well as for commercial purposes [16–23]. Our group at Seoul National University (SNU) also developed the first silicon photomultiplier (SiPM)-based PET insert that can be

Table 1. Main specifications of the SimPET scanner

		SimPET
Detector	Scintillator material	LSO
	Crystal size (mm^3)	1.2 × 1.2 × 10
	Crystal pitch (mm)	1.28
	SiPM array	4 × 4
System	No. of crystal rings	36
	No. of crystals/ring	144
	Detector face to face (mm)	63
	Axial FOV (mm)	55
	Overall dimensions Φ (cm) × L (cm)	99 × 61.5

SiPM silicon photomultiplier, *FOV* field-of-view

fully operated inside a small-animal dedicated ultra-high field MRI [24, 25]. We demonstrated the usefulness of the PET insert by conducting various multiparametric PET/MRI studies in mice [24]. However, the prototype scanner (SNU PET insert) had several limitations, including relatively low sensitivity (peak sensitivity of 3.36 % with 250–750 keV energy window) and count rate performance (peak noise equivalent count rate (NECR) of 42.4 kcps at 15.2 MBq). We recently developed SimPET (Brightonix Imaging Inc., Seoul, South Korea), the commercial version of the SNU

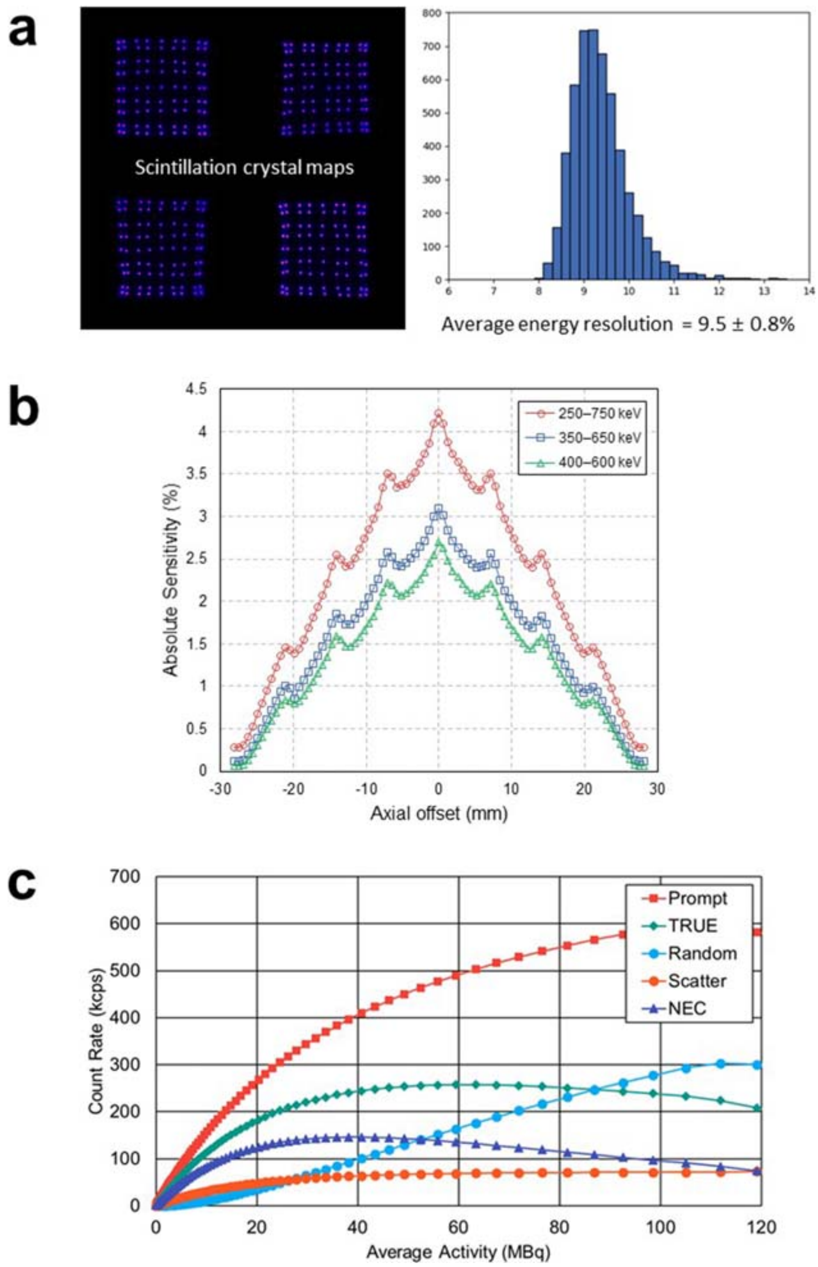

Fig. 2. Performance of SimPET. **a** Representative flood maps of the SimPET scanner and one-dimensional histogram of energy resolutions of every scintillator. **b** Axial sensitivity profiles at the center of the transaxial field-of-view. **c** Count rates of different event types as a function of the total activity within the NEMA mouse-like phantom (energy window = 250–750 keV, time window = 8 ns). Peak NECR was 150.6 kcps at 38.4 MBq, and the scatter fraction was 22.0 %.

Table 2. Spatial resolution of the SimPET scanner obtained using 3D OSEM reconstruction algorithm measured using ^{22}Na point source with no warm background

	$r = 0$ mm		$r = 5$ mm		$r = 10$ mm		$r = 15$ mm		$r = 20$ mm	
	FWHM (mm)	FWTM (mm)†	FWHM (mm)	FWTM (mm)	FWHM (mm)	FWTM (mm)	FWHM (mm)	FWTM (mm)	FWHM (mm)	FWTM (mm)
At axial center										
Radial	0.70	1.77	1.06	2.37	1.41	3.19	2.42	4.02	3.39	5.38
Tangential	0.85	1.75	0.82	1.77	0.83	1.81	0.87	1.91	0.95	2.16
Axial	1.06	3.24	1.05	3.31	1.03	3.20	1.06	3.23	0.99	2.84
At 1/4 axial FOV from center										
Radial	0.72	1.67	1.02	2.35	1.41	3.19	2.21	3.99	3.47	5.55
Tangential	0.82	1.66	0.79	1.73	0.81	1.78	0.81	1.80	0.86	1.92
Axial	0.85	2.17	0.98	2.40	0.93	2.46	0.98	2.56	0.92	2.55

FWHM full width at half maximum, *FWTM* full width at tenth maximum, *FOV* field-of-view

PET insert, with a focus on the improvement of sensitivity, count rate performance, and engineering stability.

In this study, we measured the National Electrical Manufacturers Association NU 4-2008 [26] performance characteristics of the SimPET system and compared the results with those of the SNU PET insert. In addition, we investigated the compatibility between the SimPET and M7 MRI scanner of Aspect Imaging Inc. (Shoham, Israel) and obtained simultaneous PET/MRI images of mice using the combined PET/MRI system based on SimPET and M7.

Materials and Methods

SimPET/M7 System

The SimPET scanner comprised 64 detector blocks, yielding an inner diameter of 63 mm with 16 detector blocks per ring and an axial length of 55 mm with four block rings. The PET system was covered by inner and outer carbon fibers to shield the system from electromagnetic waves and visible light [27]. The bore size was 60 mm, and the outer diameter was 99 mm; these dimensions are suitable for the PET to be inserted into MRI systems with a small opening. Axial field-of-view (FOV) of the PET scanner is 55 mm and transaxial FOV is 50 mm. Each detector block consisted of a 9 × 9 LSO crystal array and a 16-channel SiPM (S13361-3050NE-04; Hamamatsu Photonics K.K., Japan), as depicted in Fig. 1. The crystal pixel dimension was 1.2 × 1.2 × 10 mm^3. Gain variation of SiPMs caused by temperature fluctuation was compensated in real-time using a bias voltage compensation circuit. The number of readout channels were reduced by applying bipolar multiplexers [28]. Analog signals were digitized using analog-to-digital converters (ADCs) with 125 MSPS and then transferred to the field-programmable gate array-based data acquisition system. Prompt and delayed coincidences were extracted and transferred to the workstation through 1-Gbps Ethernet [29]. The energy and coincidence time windows used in this study were 350–650 keV and 8 ns, respectively. The PET images were reconstructed using a graphics processing unit (GPU)-based three-dimensional ordered-subset expectation-maximization (3D OSEM) with 3 iterations and 12 subsets. The image matrix was 160 × 160 × 86 with a voxel size of 0.32 × 0.32 × 0.64 mm^3. Component-based normalization was applied. The attenuation effect of the coil and the bed was corrected using a μ-map template acquired from a separate CT scan. Attenuation correction of the animal body was performed based on a three-segment (air, lung, and tissue) μ-map obtained from the simultaneously acquired MR images. The number of random events was estimated from the number of delayed coincidences. The SimPET specifications are summarized in Table 1.

The M7 scanner is a preclinical MRI system based on a 1-T permanent magnet from Aspect Imaging. The imaging

Table 3. Spatial resolution of the SimPET scanner obtained using 3D OSEM reconstruction algorithm using ^{22}Na point source with 10 % warm background

	$r = 0$ mm		$r = 5$ mm		$r = 10$ mm		$r = 15$ mm		$r = 20$ mm	
	FWHM (mm)	FWTM (mm)	FWHM (mm)	FWTM (mm)	FWHM (mm)	FWTM (mm)	FWHM (mm)	FWTM (mm)	FWHM (mm)	FWTM (mm)
At axial center										
Radial	1.45	3.30	1.51	3.30	1.71	3.50	2.34	4.14	3.15	5.09
Tangential	1.45	3.29	1.39	3.04	1.34	3.01	1.38	3.19	1.71	4.78
Axial	1.34	2.98	1.36	3.01	1.34	2.93	1.38	2.96	1.31	2.52
At 1/4 axial FOV from center										
Radial	1.43	3.15	1.45	3.11	1.66	3.54	2.32	4.18	3.01	5.35
Tangential	1.38	3.06	1.32	2.88	1.34	3.05	1.34	3.05	1.53	4.27
Axial	1.29	2.53	1.21	2.46	1.27	2.52	1.24	2.48	1.21	2.47

FWHM full width at half maximum, *FWTM* full width at tenth maximum, *FOV* field-of-view

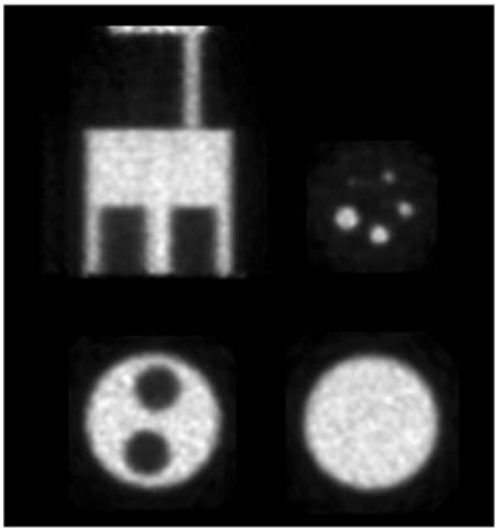

Fig. 3. Reconstructed images of the NEMA NU-4 image quality phantom.

volume of the MRI scanner was 120 × 120 × 70 mm^3 spheroid. An advantage of using a permanent magnet is that no cryogens or compressors are required to cool the magnet down. In addition, no additional shielding infrastructure is necessary because of the self-shielded magnetic field. A schematic drawing of the cross-sectional view of PET/MRI system with the major sizes is shown in Fig. 1c.

Performance Evaluation

Spatial Resolution

A ^{22}Na point source (0.74 MBq in April 2019) embedded in an acrylic cube of 10.0 mm was used for the measurement. Data were acquired with the source located at the center of the scanner and then radially stepped until 15 mm with a step size of 5 mm. The acquisitions were repeated at the same radial positions at one-fourth of the axial FOV. The PET data were reconstructed using 3D OSEM (3 iterations and 12 subsets). The spatial resolutions (FWHM and FWTM) were calculated using the method specified in NEMA NU4-2008 [26]. In addition, the calculation of spatial resolution was repeated after adding 10 % warm background (ratio of point source peak and background is 10:1 in reconstructed image).

Sensitivity

Sensitivity was also measured using a ^{22}Na point source. The source was placed at the center of the transaxial FOV and axially stepped with a 0.64-mm step size for the entire axial coverage of the scanner. The background rate was measured without the source and then subtracted from each measured count rate. The sensitivity was measured at three different energy windows: 250–750 keV, 350–650 keV, and 400–600 keV.

Count Rate Performance

The count rate performance was also measured at three different energy windows: 250–750 keV, 350–650 keV, and 400–600 keV. The coincidence time window was fixed at 8 ns. A line source inserted in a mouse-like phantom (25 mm diameter × 70 mm long) was used as specified in the NU4-2008 standard. The line source was filled with > 120 MBq ^{18}F-FDG, and all data were acquired for 10 min at every 10 min. The number of random coincidences was estimated from the number of delayed coincidence pairs. The scatter fraction was calculated using the data acquired when the random event rate was below 1 % of the true event rate. The intrinsic count rate was measured with the same phantom but without any activity in the line source.

Image quality phantom

The NEMA NU4 Image Quality phantom was scanned to estimate the quality of reconstructed images and the performance of data corrections. The acquisition and analysis were performed following the method specified in NEMA NU-42008. The default reconstruction parameters were used.

Hot Rod Phantom Study

A hot rod phantom with an inner diameter of 28 mm and a height of 27.5 mm was scanned to evaluate the spatial

Table 4. Image quality results obtained from the reconstructed image of NEMA NU-4 image quality phantom

Parameter	Value				
Uniformity	Mean	Maximum	Minimum	%STD	
	5.48	6.34	4.62	4.42	
RC	1 mm	2 mm	3 mm	4 mm	5 mm
	0.17 (12.3)	0.52 (6.87)	0.75 (7.03)	0.85 (6.06)	0.90 (6.34)
Accuracy of correction	Water-filled cylinder		Air-filled cylinder		
	SOR	%STD	SOR	%STD	
	0.15	14.6	0.13	12.7	

STD standard deviation; *RC* recovery coefficient, mean (%SD); *SOR* spillover ratio

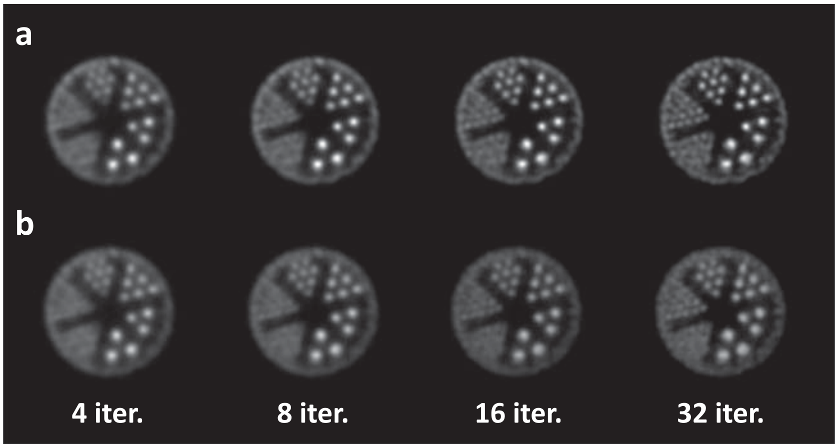

Fig. 4. Reconstructed images of the hot rod phantom with rod diameters of 0.75, 1, 1.35, 1.7, 2.0, and 2.4 mm using 3D OSEM algorithm **a** with the incorporation of point spread function (PSF), and **b** without PSF incorporation.

resolving performance of the PET scanner. The phantom had six groups of rods with diameters of 0.75, 1.0, 1.35, 1.7, 2.0, and 2.5 mm. The center-to-center spacing of each rod was two times its diameter. The phantom was filled with 4.48 MBq of ^{18}F-FDG and scanned for 30 min. Images were reconstructed using the 3D OSEM algorithm with and without incorporating the point spread function (32 iterations and 15 subsets) [30]. Attenuation was corrected using the registered attenuation map acquired from a separate CT scan.

MRI-Compatibility Measurement

A uniform corn oil phantom was scanned using an M7 MRI scanner with several different pulse sequences, such as three-dimensional gradient-echo (GRE), T1-weighted spin-echo (T1WSE), and T2-weighted fast spin-echo (T2WFSE). The MR images were acquired without and with PET (power off and on) inside the MR scanner. The SNR and integral uniformity of the MR images were calculated according to our previous study [24].

To assess the influence of MRI on the PET images, PET scan data were also acquired while the PET insert was installed inside the M7 MRI. The count rate variation under GRE, T1WSE, and T2WFSE MRI pulse sequences was investigated. Blank count rates with no positron source inside of the PET and count rates with ^{22}Na point source at FOV center were measured.

Animal Imaging Experiments

All animal experiments were approved by the Institutional Animal Care and Use Committee at the SNU Hospital. The mice were anesthetized with isoflurane (1.5–3 % in air) and positioned in a heated animal handling system during image acquisition.

Mouse Whole-Body PET Study

A mouse whole-body PET study was performed on a C57BL/6 mouse (male, 9 weeks old, 20.4 g) 30 min after intravenous injection of 9.58 MBq ^{18}F-NaF. Two-bed position with an overlap of 9.6 mm was used to yield the total axial FOV of 96.64 mm. The scan time for each bed position was 20 min.

Simultaneous PET/MRI Study

A simultaneous PET/MRI study was conducted on BALB/c mouse (male, 6 weeks old, 20.5 g) with ^{64}Cu-NOTA-ironoxide with 5-nm core size developed as a multimodal vascular imaging agent. Ten minutes after intravenous injection of 12.0 MBq ^{64}Cu-NOTA-ironoxide, list-mode PET and T1-weighted MRI (TR/TE, 9/2.8 ms; FA, 45°, 25 slices) images were simultaneously acquired for 6 min. These images were compared with T1-weighted MRI images acquired using the same MRI protocol before the radiotracer injection.

Results

Intrinsic Performance

Every LSO scintillation crystal was well resolved, as shown in the flood maps of some representative crystal blocks (Fig. 2a). The average energy resolution of the scanner was 9.5 ± 0.8 %. The one-dimensional histogram of the energy resolutions is also shown in Fig. 2a.

Spatial Resolution

The radial spatial resolution measured without the warm background was 0.70 mm FWHM (1.77 mm FWTM) at the center of the scanner, and 2.42 mm FWHM (4.02 mm

FWTM) at 15 mm radial offset. The spatial resolution got worse when it was measured using point source in warm background. The radial spatial resolution measured with 10 % warm background was 1.45 mm FWHM (3.30 mm FWTM) at the center of the scanner, and 2.34 mm FWHM (4.14 mm FWTM) at 15 mm radial offset. The spatial resolutions at different radial and axial locations acquired using 3D OSEM algorithm without and with the warm background are summarized in Tables 2 and 3.

Sensitivity

The peak sensitivity was 4.21 % in the 250–750 keV energy window after correcting the effect of ^{176}Lu background activity and 2.70 % in the 400–600 keV energy window. The sensitivity profiles measured with different energy windows are shown in Fig. 2b.

Count Rate Performance

In the 250–750 keV energy window, the peak NECR was 151 kcps at 38.4 MBq, and the peak true count rate was 265 kcps at 59.7 MBq. The scatter fraction was 22.0 %. The count rate curves measured in the 250–750 keV energy window are plotted in Fig. 2c, and those in the other energy windows are in Supplemental Figs. 1 and 2.

Image Quality

The reconstructed images of the NEMA NU-4 image quality phantom are shown in Fig. 3. The uniformity was 4.42 %, and the average spillover-ratio was 0.14. The recovery coefficient (RC) was over 75 % in the 3-mm rod. Detailed results are summarized in Table 4.

Phantom Imaging Study

In the hot rod phantom image reconstructed using 3D OSEM algorithm with the incorporation of point spread function, > 1-mm rods were clearly separated from each other and even the smallest rods (*i.e.*, 0.75 mm diameter) were distinguishable, as shown in Fig. 4a. The images reconstructed using 3D OSEM without resolution recovery using point spread function are shown in Fig. 4b. Slice thickness of these images were 0.64 mm.

MRI Compatibility

For each pulse sequence, MR images showed almost the same SNR and uniformity regardless of the PET conditions, as summarized in Fig. 5a and b. In addition, there were no remarkable differences in PET count rates with different MRI pulse sequences (Fig. 5c).

Animal Imaging Experiments

Mouse Whole-Body PET Study

Fig. 6a shows the maximum intensity projection images of ^{18}F-NaF bone PET study conducted in C57BL/6 mouse. The images show high uptake of the radiotracer in skeletal regions. Each rib is clearly resolved, demonstrating high spatial resolution and good image quality of the SimPET scanner.

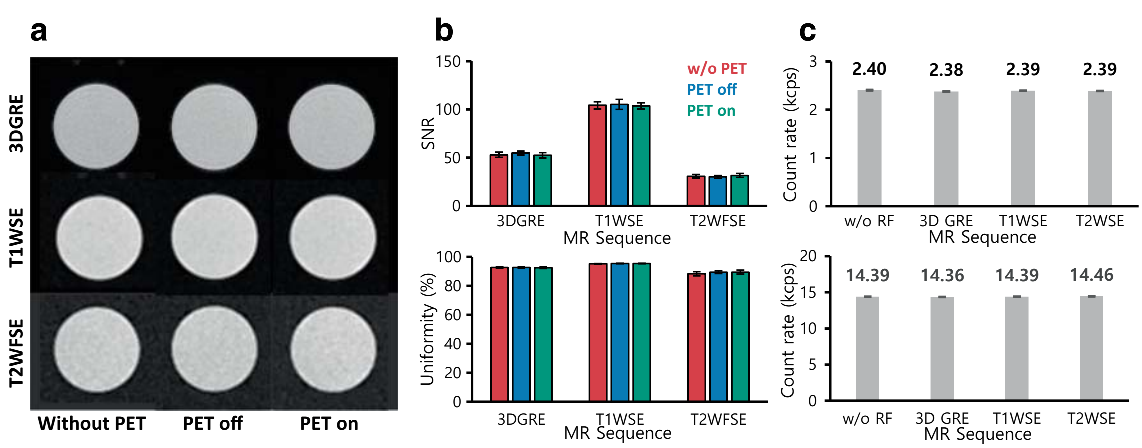

Fig. 5. MRI compatibility of SimPET. **a** MRI images of the uniform phantom obtained using three different MRI pulse sequences under different PET conditions. **b** SNR and uniformity of MRI images. **c** PET count rates (upper: blank scan, lower: with ^{22}Na source at FOV center) measured with different MRI pulse sequences: without RF pulse and with GRE, T1WSE, and T2WSE sequences.

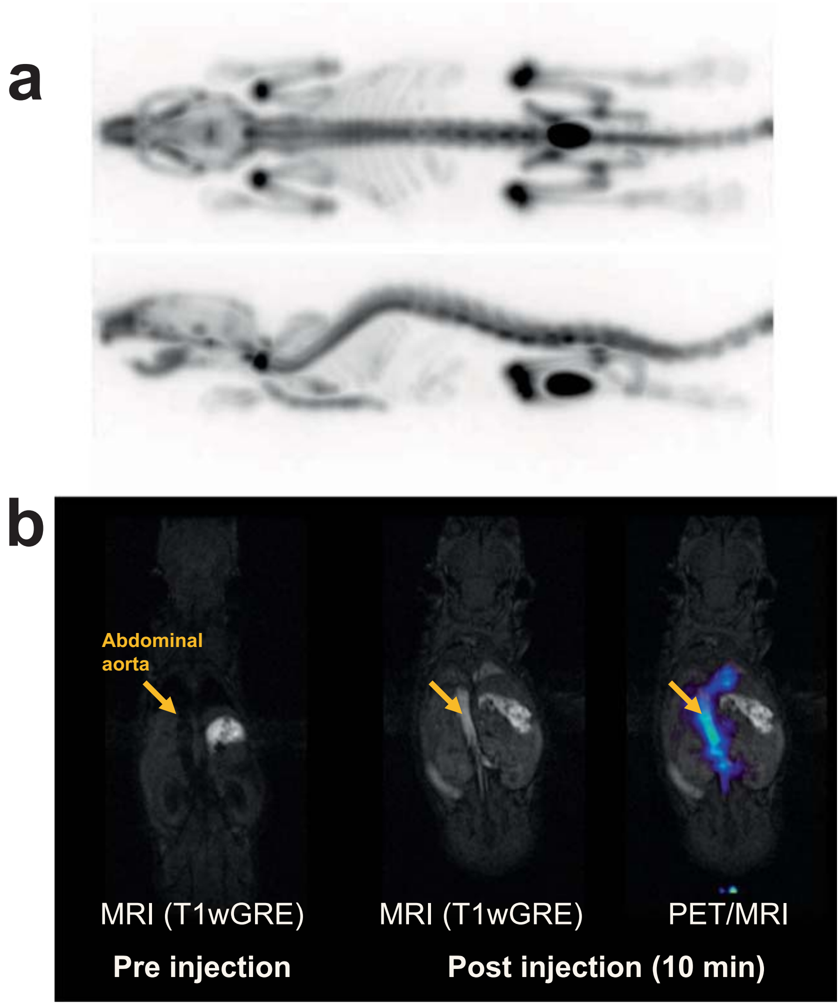

Fig. 6. Animal imaging studies. **a** ^{18}F-NaF mouse whole-body PET image (maximum intensity projection). **b** Simultaneous mouse PET/MRI images acquired before and 10 min after intravenous injection of ^{64}Cu-NOTA-ironoxide.

Simultaneous PET/MRI Study

Fig. 6b shows the T1-weighted MR and PET/MR images of a BALB/c mouse before and after injection of ^{64}Cu-NOTA-ironoxide. In the 10-min post-injection MR and PET/MR images, the signal intensity in the abdominal aorta was remarkably increased with good agreement of spatiotemporal distribution of the dual-modal imaging probe for PET and MRI.

Table 5. Summary of PET performance measurement of the SimPET scanner and its prototype (SNU PET insert)

		SimPET	SNU prototype [25]
Volumetric resolution	OSEM (mm^3)	0.63	0.53
Sensitivity	250–750 keV (%)	4.21	3.36
	350–650 keV (%)	3.10	2.50
	400–600 keV (%)	2.70	2.11
Count rate performance	Peak NECR (kcps)	151	42.4
	Activity at peak NECR (MBq)	38.4	15.2
	Scatter fraction (%)	22.0	16.5
Image quality	Uniformity (%)	4.42	6.19
	RC at 1-, 2-, 3-, 4-, and 5-mm rod diameter	0.17, 0.52, 0.75, 0.85, 0.90	0.14, 0.44, 0.65, 0.90, 0.93
	SOR air (%)	12.7	17.3
	SOR water (%)	14.6	8.5

OSEM ordered-subset expectation-maximization, *NECR* noise equivalent count rate, *RC* recovery coefficient, *SOR* spillover ratio

Discussion

In this study, we evaluated the performance of the SimPET insert which is an MRI-compatible compact preclinical PET scanner with high resolution and count rate capability. To obtain simultaneous PET/MR images of small rodents, the SimPET insert was combined with a M7 MRI which is a small-bore 1-T permanent magnet-based MRI system requiring no cryogen, compressor, and RF shielding room. One of the main advantages of this SimPET/M7 combination is that the combined system needs a small space (less than 9 m^2) for installation of all the equipment for simultaneous PET/MR imaging (PET/MRI scanner, electronic cabinets, operating computers, and gas anesthesia/physiological monitoring devices). The results of NEMA performance measurement demonstrated the fine imaging performance of the SimPET scanner. For example, in the hot rod phantom image reconstructed using 3D OSEM with point spread function, the smallest rods (*i.e.*, 0.75 mm diameter) were distinguishable from each other, indicating that the SimPET system can resolve submillimeter structures in mice and rats.

The physical performance of the SimPET system was remarkably improved when compared to its prototype (SNU PET insert), as summarized in Table 5. The peak NECR was improved more than three times from 42.4 kcps (at 15.2 MBq) to 151 kcps (at 38.4 MBq). Another major enhancement was the sensitivity, which increased from 3.36 to 4.21 % in the energy window of 250–750 keV. The primary reason for the improvement was the advancement of analog and digital electronics used in the SimPET system. The current driving capability of the integrated circuits was increased to reinforce high count rate support. Furthermore, the performance of the online coincidence module was improved not to lose any valid coincidence pairs even under high activity conditions.

As demonstrated in the simultaneous PET/MRI study with ^{64}Cu-NOTA-ironoxide, the SimPET/M7 scanner can serve as a tool for investigating multimodal imaging probes by providing complementary characteristics (*i.e.*, high sensitivity of PET and high resolution of MRI) with exact spatiotemporal correlation. Furthermore, other preclinical studies that require both functional and morphological information with good soft-tissue contrast and spatiotemporal correlation [31–33] will benefit from the simultaneous PET/MRI system.

Although the PET scanner has limited axial length (*i.e.*, 55 mm), whole-body mouse scan was possible by stitching the two images of different bed positions, as demonstrated in Fig. 6a. Mice with axial length up to 82.5 mm can be scanned using two-bed positions with overlap of 13.75 mm.

Conclusions

Our results proved the high count rate performance as well as the excellent spatial resolution of the SimPET system which are essential for obtaining high-quality images of radiopharmaceutical concentration in small animals. The combined SimPET/M7 enabled simultaneous PET/MR imaging with no remarkable mutual interference between the two imaging modalities. The developed imaging system therefore will be advantageous for investigating rodent models of diseases and developing new multimodal imaging probes.

Funding. This work was supported in part by grants from the Seoul National University Creative Factory funded by the Korean Ministry of SMEs and Startups (grant no. 10080715).

Compliance with Ethical Standards

Ethical Approval

All animal experiments were approved by the Institutional Animal Care and Use Committee at the Seoul National University Hospital.

Conflict of Interest

J-W Son, KY Kim, K Kim, GB Ko, and JS Lee are employees of Brightonix Imaging Inc.

References

1. Rudin M, Weissleder R (2003) Molecular imaging in drug discovery and development. Nat Rev Drug Discov 2:123–131
2. Koo V, Hamilton PW, Williamson K (2006) Non-invasive *in vivo* imaging in small animal research. Cell Oncol 28:127–139
3. Kim C, Chen Z (2018) Multimodal photoacoustic imaging: systems, applications, and agents. Biomed Eng Lett 8:137–138
4. Son H, Jang K, Lee H, Kim SE, Kang KW, Lee H (2019) Use of molecular imaging in clinical drug development: a systematic review. Nucl Med Mol Imaging 53:208–215
5. Choi WJ (2019) Optical coherence tomography angiography in preclinical neuroimaging. Biomed Eng Lett 9:311–325
6. Cassidy PJ, Radda GK (2005) Molecular imaging perspectives. J R Soc Interface 2:133–144
7. Pichler BJ, Wehrl HF, Judenhofer MS (2008) Latest advances in molecular imaging instrumentation. J Nucl Med 49:5S–23S
8. Vaska P, Rubins DJ, Alexoff DL, Schiffer WK (2006) Quantitative imaging with the micro-PET small-animal PET tomograph. Int Rev Neurobiol 73:191–218
9. Antoch G, Bockisch A (2009) Combined PET/MRI: a new dimension in whole-body oncology imaging? Eur J Nucl Med Mol Imaging 36(Suppl 1):S113–S120
10. Jadvar H, Colletti PM (2014) Competitive advantage of PET/MRI. Eur J Radiol 83:84–94
11. Yoo HJ, Lee JS, Jee JM (2015) Integrated whole body PET/MRI: where are we? Korean J Radiol 16:32–49
12. Lee DS (2019) Clinical personal connectomics using hybrid PET/MRI. Nucl Med Mol Imaging 53:153–163
13. Judenhofer MS, Wehrl HF, Newport DF, et al (2008) Simultaneous PET-MRI: a new approach for functional and morphological imaging. Nat Med 14:459–465
14. Schlemmer HPW, Pichler BJ, Schmand M, et al (2008) Simultaneous MR/PET imaging of the human brain: feasibility study. Radiology 248:1028–1035
15. Catana C, Drzezga A, Heiss W-D, Rosen BR (2012) PET/MRI for neurologic applications. J Nucl Med 53:1916–1925
16. Yoon HS, Ko GB, Kwon SI, et al (2012) Initial results of simultaneous PET/MRI experiments with an MRI-compatible silicon photomultiplier PET scanner. J Nucl Med 53:608–614
17. Omidvari N, Cabello J, Topping G et al (2017) PET performance evaluation of MADPET4: a small animal PET insert for a 7T MRI scanner. Phys Med Biol 62:8617–8692

18. Stortz G, Thiessen JD, Bishop D et al (2018) Performance of a PET insert for high-resolution small-animal PET/MRI at 7 tesla. J Nucl Med 59:536–542
19. Hallen P, Schug D, Weissler B et al (2018) PET performance evaluation of the small-animal Hyperion II^{D} PET/MRI insert based on the NEMA NU-4 standard. Biomed Phys Eng Express 4:065027
20. Yamamoto S, Watabe T, Watabe H, et al (2012) Simultaneous imaging using Si-PM-based PET and MRI for development of an integrated PET/MRI system. Phys Med Biol 57:N1–N13
21. Chang CM, Lee BJ, Grant AM, Groll AN, Levin CS (2018) Performance study of a radio-frequency field-penetrable PET insert for simultaneous PET/MRI. IEEE Trans Radiat Plasma Med Sci 2:422–431
22. Belcari N, Bisogni MG, Camarlinghi N et al (2019) Design and detector performance of the PET component of the TRIMAGE PET/MR/EEG scanner. IEEE Trans Radiat Plasma Med Sci 3:292–3011
23. Gonzalez AJ, Gonzalez-Montoro A, Vidal LF et al (2019) Initial results of the MINDView PET insert inside the 3T mMR. IEEE Trans Radiat Plasma Med Sci 3:343–351
24. Ko GB, Yoon HS, Kim KY, et al (2016) Simultaneous multi-parametric PET/MRI with silicon photomultiplier PET and ultra-high field MRI for small animal imaging. J Nucl Med 57:1309–1315
25. Ko GB, Kim KY, Yoon HS et al (2016) Evaluation of a silicon photomultiplier PET insert for simultaneous PET and MR imaging. Med Phys 43:72–83
26. National Electrical Manufacturers Association (2007) NEMA standards publication NU 2–2007: performance measurements of positron emission tomographs. National Electrical Manufacturers Association, Rosslyn
27. Peng BJ, Wu Y, Cherry SR, Walton JH (2014) New shielding configurations for a simultaneous PET/MRI scanner at 7T. J Magn Reson 239:50–56
28. Yoon HS, Lee JS (2014) Bipolar analog signal multiplexing for position-sensitive PET block detectors. Phys Med Biol 59:7835–7846
29. Son J-W, Won JY, Lee JS (2017) Evaluation of a FPGA-based real-time coincidence system for high count rate PET scanners. IEEE Nucl Sci Sym Med Imaging Conf Conference Record. https://doi.org/10.1109/NSSMIC.2017.8533051
30. Panin VY, Kehren F, Michel C, Casey M (2006) Fully 3-D PET reconstruction with system matrix derived from point source measurements. IEEE Trans Med Imaging 25:907–921
31. Uppal R, Catana C, Ay I, Benner T, Sorensen AG, Caravan P (2011) Bimodal thrombus imaging: simultaneous PET/MR imaging with a fibrin-targeted dual PET/MR probe—feasibility study in rat model. Radiology 258:812–820
32. Ng TSC, Bading JR, Park R, et al (2012) Quantitative, simultaneous PET/MRI for intratumoral imaging with an MRI-compatible PET scanner. J Nucl Med 53:1102–1109
33. Goldenberg JM, Cardenas-Rodriguez J, Pagel MD (2018) Preliminary results that assess metformin treatment in a preclinical model of pancreatic cancer using simultaneous [^{18}F]FDG PET and acidoCEST MRI. Mol Imaging Biol 20:575–583